WCI3, February 12-16 2005, TAMU

Statistical descriptions of nuclear decay

A.S. Botvina

Institute for Nuclear Research, Russian Academy of Sciences, Moscow, Russia

- 1. Development of the statistical approach for description of equilibrium stages of the nuclear reactions
- 2. Statistical multifragmentation models and their results
- 3. Comparison of experimental data with the statistical models and extraction of relevant physical information
- 4. Applications of statistical nuclear multifragmentation and its connection with other physical processes

Statistical approach in nuclear reactions: conception of equilibrium

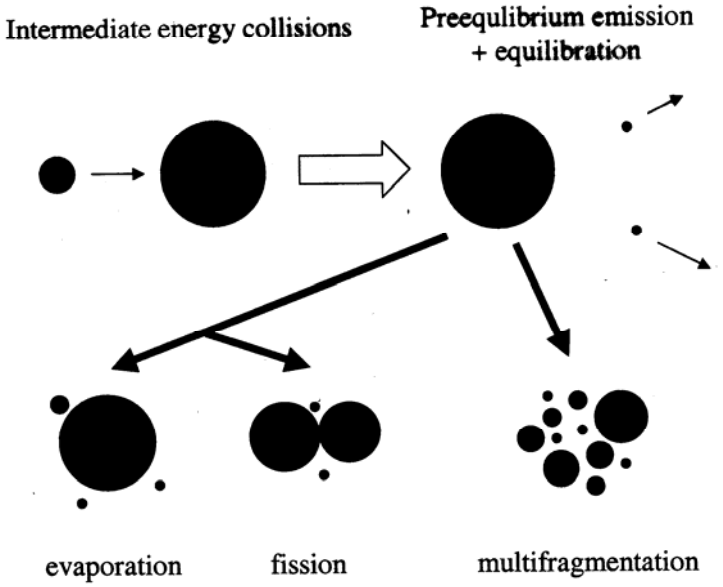

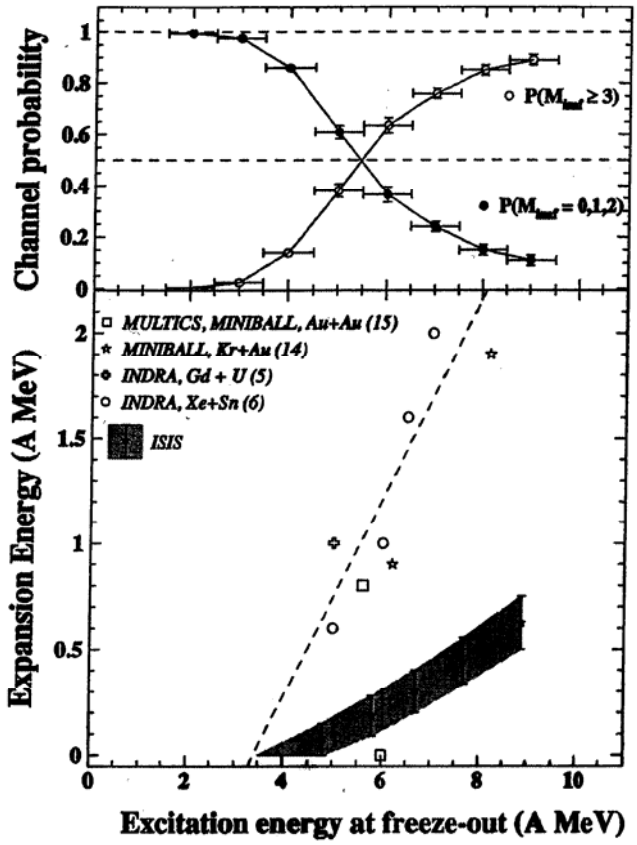

FIG. 4. Upper panel: decay channel probability as a function of the excitation energy, corrected for detector efficiency. The horizontal errors correspond to the excitation energy bin width; the vertical ones represent two assumptions regarding the detector efficiency. Lower panel: comparison between 8 GeV/c $\pi^- + {}^{197}$Au reactions and central heavy-ion collisions. The shaded area corresponds to the ISiS expansion energies extracted with SMM at $3V_0$ (upper limit) and $2V_0$ (lower limit). The dashed line summarizes the expansion energies extracted in central heavy-ion collisions with various assumptions regarding the source characteristics. See [5,6,14,15] for more details.

Foundation of the statistical approach in nuclear physics:

Niels Bohr conception of the compound nucleus, 1936

Weisskopf evaporation approach, 1937

Bohr-Wheeler fission approach, 1939

Fermi theory of the multiple particle production, 1950

Development of evaporation/fission:

Hauser-Feshbach evaporation model, 1952

Fong statistical fission model, 1956

.....

Dubna evaporation/fission models, 1960–1970

Blann preequilibrium/evaporation model, 1970–1980

Moretto evaporation/fission model, 1970–1980

.....

Development of statistical multifragmentation 1980–1990:

A.Z.Mekjian, Phys. Rev. **C17**, 1051 (1978)

QSM: D.Hahn, and H.Stoecker, Nucl. Phys. **A476**, 718 (1988)

EES: W.A.Friedman, Phys. Rev. **C42**, 667 (1990)

Randrup (FREESCO, WIX):

J.Randrup, and S.E.Koonin, Nucl. Phys. **A356**, 223 (1981)

G.Fai, and J.Randrup, Nucl. Phys. **A404**, 551 (1983)

S.E.Koonin, and J.Randrup, Nucl. Phys. **A474**, 173 (1987)

J.Randrup, Comp. Phys. Comm. **77**, 153 (1993)

MMMC:

D.H.E.Gross et al., Z. Phys. **A309**, 41 (1982)

X.Z.Zhang, D.H.E.Gross et al., Nucl. Phys. **A461**, 641 (1987)

D.H.E.Gross, and H.Massmann, Nucl. Phys. **A471**, 339c (1987)

D.H.E.Gross, Rep. Prog. Phys. **53**, 605 (1990)

SMM:

J,P.Bondorf, R.Donangelo, I.N.Mishustin, C.J.Pethick, H.Schulz, and K.Sneppen, Nucl. Phys. **A443**, 321 (1985)

J.P.Bondorf, R.Donangelo, I.N.Mishustin, and H.Schulz, Nucl. Phys. **A444**, 460 (1985)

K.Sneppen, Nucl. Phys. **A470**, 213 (1987)

A.S.Botvina, A.S.Iljinov, I.N.Mishustin, Sov. J. Nucl. Phys. **42**, 712 (1985)

A.S.Botvina, A.S.Iljinov, and I.N.Mishustin, JETP Lett. **42**, 572 (1985)

A.S.Botvina, A.S.Iljinov, and I.N.Mishustin, Nucl. Phys. **A507**, 649 (1990)

J.P.Bondorf, A.S.Botvina, A.S.Iljinov, I.N.Mishustin, and K.Sneppen, Phys. Rep. **257**, 133 (1995)

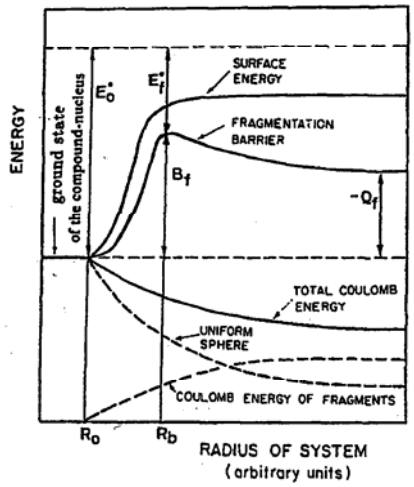

Fig. 3.1. The qualitative representation of different contributions to the total energy of a nuclear system undergoing multifragmentation versus its radius R. The sum of surface and Coulomb energies has a characteristic bechaviour with a potential barrier.

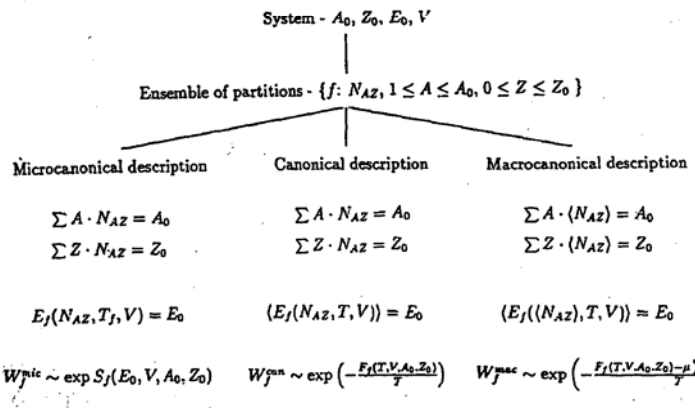

Fig. 2.2. Schematic classification of statistical ensembles used for describing break-up of the nuclear system with mass number A_0, charge Z_0 and total energy E_0 in a volume V.

Isospin of fragments in Statistical Multifragmentation Model (in Grand-canonical appr.)

Average multiplicity of fragments with mass number A and charge Z (J.P.Bondorf et al., Phys. Rep. 257 (1995)):

$$\langle N_{AZ}\rangle = g_{AZ}\,\frac{V_f}{\lambda_T^3}\,A^{3/2}\cdot\exp\left[-\frac{1}{T}\left(F_{AZ}(T,\rho)-\mu A-\nu Z\right)\right],$$

where T - temperature, λ_T - thermal wavelength, g_{AZ} - degeneracy, F_{AZ} - internal free energy of the fragment, V_f - "free" volume, μ and ν - chemical potentials responsible for charge and mass conservation.

The charge distribution of fragments with given A (A.S.Botvina et al. Nucl.Phys. A475 (1987) 663):

$$N_A(Z) \sim \exp\left[-(Z-\langle Z_A\rangle)^2/2(\sigma_Z^A)^2\right],$$

the charge dispersion:

$$\sigma_Z^A \simeq \sqrt{AT/8\gamma},$$

the average charge:

$$\langle Z_A\rangle = \frac{(4\gamma+\nu)\cdot A}{8\gamma+2c\cdot A^{2/3}},$$

where $\gamma \approx 25$ MeV - the symmetry energy coefficient, $c = (3/5)\cdot(e^2/r_0)\cdot(1-(\rho/\rho_0)^{1/3})$ - Coulomb energy parameter in Wigner-Seitz approximation, ρ - the nuclear density at freeze-out.

A. S. Botvina, A. S. Il'inov, and I. N. Mishustin[1)]

Sov. J. Nucl. Phys. 42 (5), November 1985

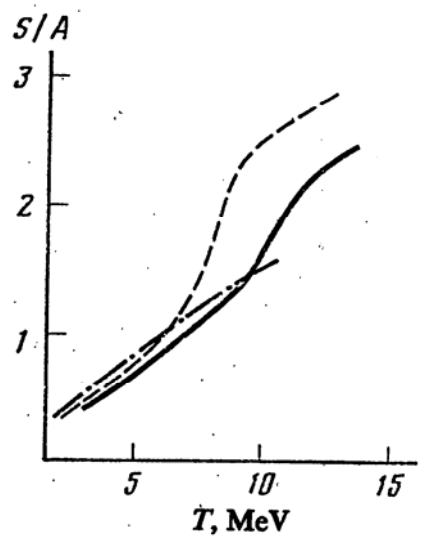

FIG. 1. Entropy S/A of the compound nucleus (dot-dash) and of the multifragment nuclear system (solid curve—$\varkappa = 0.1$ and dashed curve—$\varkappa = 1.0$) as functions of the temperature T. The calculation was made for a nucleus $A_0 = 220$, $Z_0 \mp 86$ with a parameter $\varepsilon_0 = 16$ MeV.

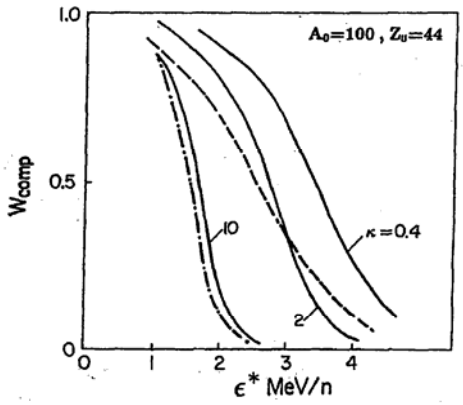

Fig. 5.5. Survival probability of the compound-nucleus W_{comp} versus the excitation energy of the decaying system with $A_0 = 100$, $Z_0 = 44$. The solid curves correspond to the microcanonical calculation with the $\epsilon_0 = 16$ MeV and different values of κ given in the figure. The dashed curve shows the canonical calculation with $\epsilon_0 = 16$ MeV and $\kappa = 2$. The dot-dashed curve is the microcanonical calculation with $\epsilon_0 = 40$ MeV and $\kappa = 2$.

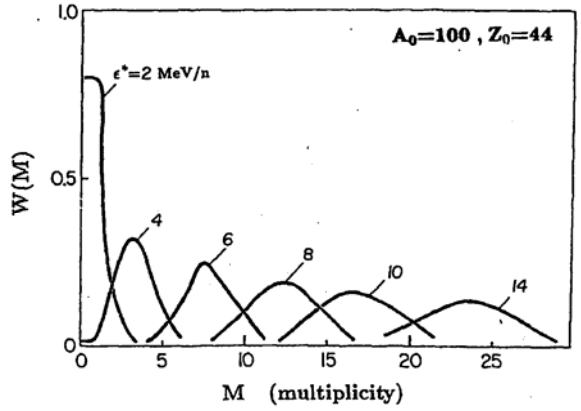

Fig. 5.4. Microcanonical calculation of the M-fragment break-up probability $W(M)$ for the system with $A_0 = 100$ and $Z_0 = 44$. The numbers near the curves give the excitation energy in MeV/nucleon. The parameters: $\epsilon_0 = 16$ MeV and $\kappa = 2$.

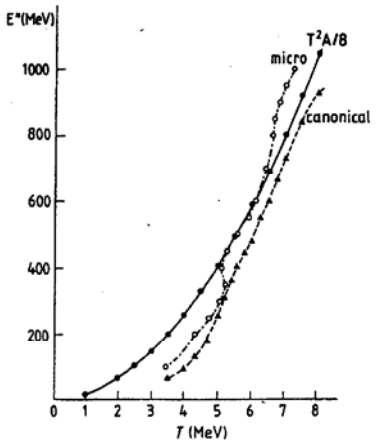

Figure 3. Canonical and microcanonical $T(E^*)$ for ^{131}Xe. To compare both calculations, the depth of the neutron potential V_0 (cf section 7.2.1) was put to zero in the microcanonical calculation.

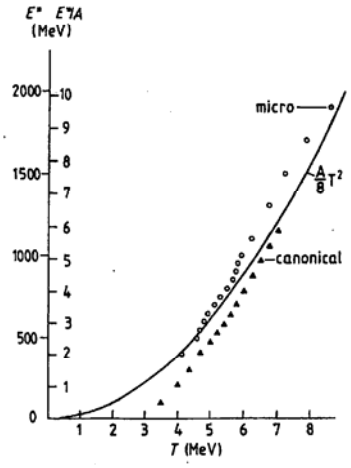

Figure 4. The same as in figure 3, but for ^{197}Au.

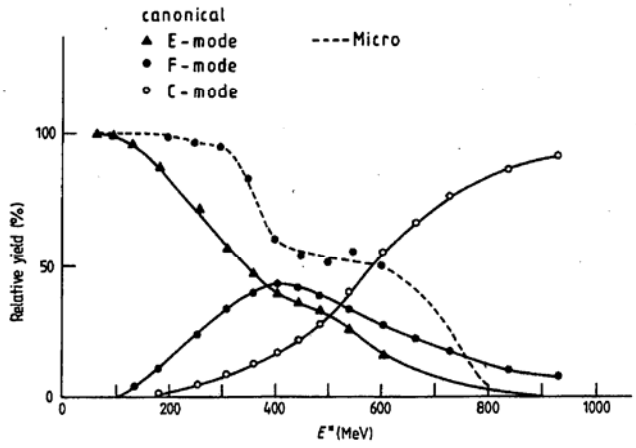

Figure 5. Heavy mass correlation for ^{131}Xe in canonical and microcanonical sampling.

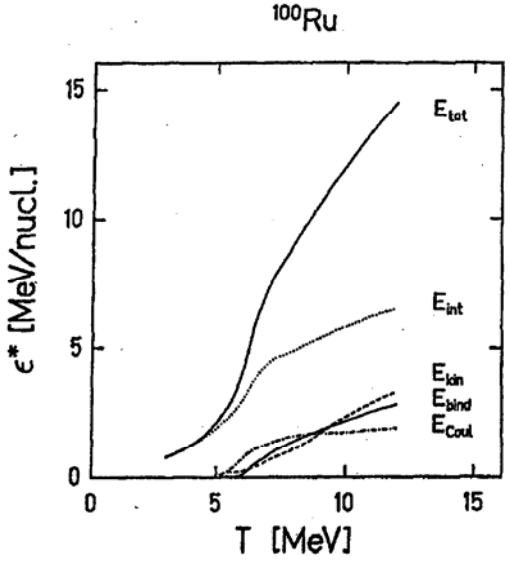

Fig. 5.3. Total excitation energy E_{tot} versus the temperature at the break-up of a ^{100}Ru nucleus ($A_0 = 100$, $Z_0 = 44$). The different contributions to the total energy are shown separately: E_{int}, internal excitation energy of fragments; E_{kin}, kinetical energy of fragments; E_{bind}, mass defect energy; E_{Coul}, Coulomb barrier energy.

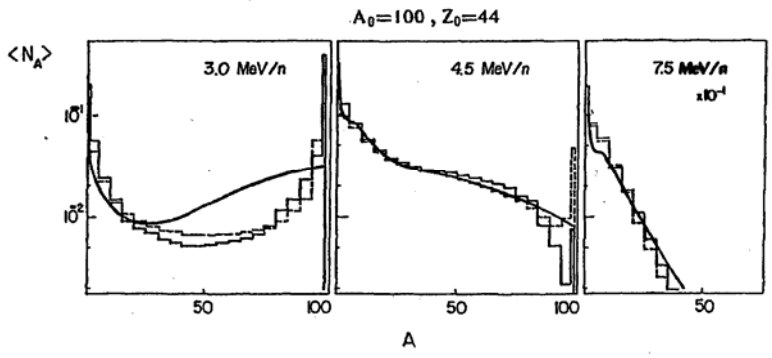

Fig. 5.6. Average multiplicity of fragments $\langle N_A \rangle$ versus the fragment mass A for the system with $A_0 = 100$, $Z_0 = 44$. The excitation energies are shown in the figure. The solid and dashed histograms are respectively microcanonical and canonical calculations. Solid curve is macrocanonical calculation.

Development of statistical models after 1990:

SIMON: D.Durand, Nucl. Phys. **A541**, 266 (1992)

MMM: Al.H.Raduta, and Ad.R.Raduta, Phys. Rev. **C55**, 1344 (1997)

Al.H.Raduta, and Ad.R.Raduta, Phys. Rev. **C61**, 034611 (2000)

ISMM: M.P.Tan et al., Phys. Rev. **C68**, 034609 (2003)

SMM: K.A.Bugaev, M.I.Gorenstein, I.N.Mishustin, and W.Greiner, Phys. Rev. **C62**, 044320 (2000)

A.S.Botvina and I.N.Mishustin, Phys. Rev. **C63**, 061601 (2001)

A.S.Botvina and I.N.Mishustin, Phys. Lett. **B584**, 233 (2004)

MMMC: D.H.E.Gross, Phys. Rep. **279**, 119 (1997)

A.S.Botvina, and D.H.E.Gross, Phys. Rev. **C58**, R23 (1998)

A.Le Fevre, M.Ploszajczak, and V.D.Toneev, Phys. Rev. **C60**, 051602 (1999)

Canonics: K.C.Chase, and A.Z.Mekjian, Phys. Rev. **C52**, R2339 (1995)

S.Das Gupta, and A.Z.Mekjian, Phys. Rev. **C57**, 1361 (1998)

S.Das Gupta, A.Z.Mekjian, and B.Tsang, Adv. Nucl. Phys. **26**, 89 (2001)

S.Pratt, W.Bauer, et al., Phys. Rev. **C63**, 034608 (2001)

A.S.Parvan, V.D.Toneev, and M.Ploszajczak, Nucl. Phys. **A676**, 409 (2000)

Comparison of statistical models with experiments:

Comparisons with active participation of experimenters:

J.Hubele et al., Phys. Rev. **C46**, R1577 (1992)

A.S.Botvina et al., Nucl. Phys. **A584**, 737 (1995)

H.Xi et al., Z. Phys. **A359**, 397 (1997)

M.D'Agostino et al., Phys. Lett. **B371**, 175 (1996)

M.D'Agostino et al., Nucl.Phys. **A650**, 329 (1999)

C.Williams et al., Phys. Rev. **C55**, 2132 (1997)

W-C.Hsi, K.Kwiatkowski, et al., Phys. Rev. **C60**, 034609 (1999)

V.E.Viola et al., Nucl. Phys. **A681**, 267 (2001)

M.Veselsky et al., Phys. Rev. **C62**, 064613 (2000)

V.K.Rodionov et al., Nucl. Phys. **A700**, 457 (2002)

N.Bellaize et al., Nucl. Phys. **A709**, 367 (2002)

A.Le Fevre et al., Nucl. Phys. **A735**, 219 (2004)

J.A.Hauger et al., Phys. Rev. **C62**, 024616 (2000)

R.P.Scharenberg, B.K.Srivastava et al., Phys. Rev. **C64**, 054602 (2001)

ALADIN

MULTICS/MINI

MINIBALL

ISiS

TAMU

FAZA

INDRA

EOS

M. D'Agostino et al.

Physics Letters B 371 (1996) 175–180

MULTICS+MINIBALL

Statistical multifragmentation in central Au + Au collisions at 35 MeV/u

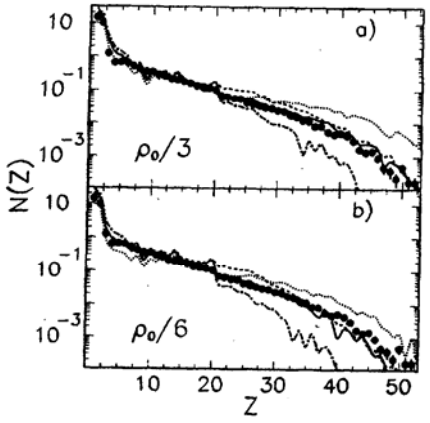

Fig. 1. Charge distribution $N(Z)$. Points show experimental data and lines show results of SMM predictions for sources with parameters $A_s = 343$, $Z_s = 138$, $E_s^*/A = 6.0$ MeV, $\rho_s = \rho_0/3$ (part a)) and $A_s = 315$, $Z_s = 126$, $E_s^*/A = 4.8$ MeV, $E_{flow}/A = 0.8$ MeV, $\rho_s = \rho_0/6$ (part b)). Dashed curves are the unfiltered calculations and solid curves are the filtered ones. The dot-dashed and dotted curves represent filtered calculations for thermal excitations $E_s^*/A + 1$ MeV/u and $E_s^*/A - 1$ MeV/u, respectively.

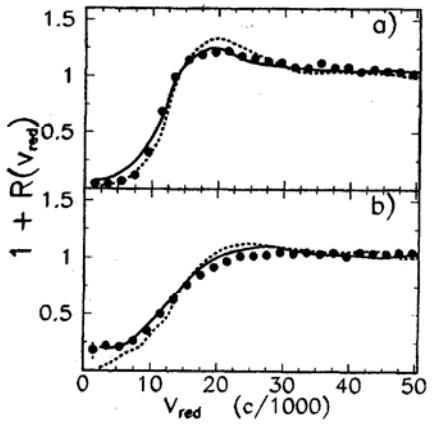

Fig. 4. Two-fragment correlation functions $1 + R(v_{red})$ for $3 \le Z \le 30$ and $8° \le \theta_{lab} < 23°$ (part a)) and for $3 \le Z \le 10$ and $23° \le \theta_{lab} \le 40°$ (part b)). Full points show experimental data. The solid and dashed lines are SMM predictions for $\rho_s = \rho_0/3$, and $\rho_s = \rho_0/6$ (other source parameters as in Fig. 1).

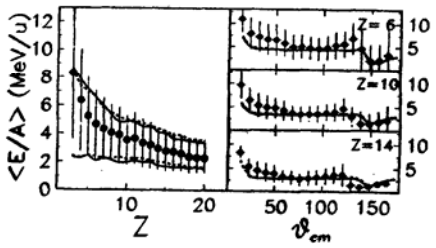

Fig. 3. Mean centre-of-mass kinetic energy per nucleon, $\langle E/A \rangle$, as a function of the charge Z, for fragments emitted at $\theta_{cm} = 90° \pm 10°$ (left panel) and (for $Z = 6, 10, 14$) as a function of θ_{cm} (right panels). Points give the experimental values of $\langle E/A \rangle$ and vertical bars give the standard deviations $\Delta E/A$ of the distributions. The solid and dashed lines are SMM predictions of $\langle E/A \rangle$ (in the left panel show the two values $\langle E/A \rangle \pm \Delta E/A$) for $\rho_s = \rho_0/3$, and $\rho_s = \rho_0/6$, respectively (other source parameters as in Fig. 1). The energy range is the same in the left and in each right panel.

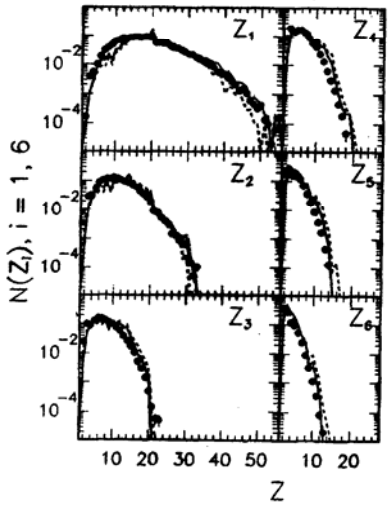

Fig. 2. Charge distribution of the six heaviest fragments, ordered such as $Z_i \ge Z_k$ if $i < k$. Experimental data are shown by points, the solid and dashed curves show the results of SMM calculations for $\rho_s = \rho_0/3$, and $\rho_s = \rho_0/6$, respectively (other source parameters as in Fig. 1).

Two-stage multifragmentation of 1*A* GeV Kr, La, and Au

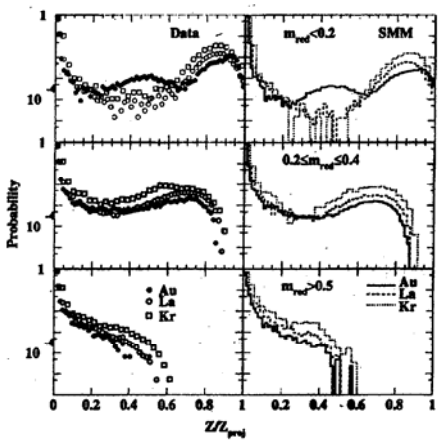

FIG. 24. Second stage fragment charge distribution as a function of $Z/Z_{projectile}$. Results are shown for three reduced multiplicity intervals for both data and SMM.

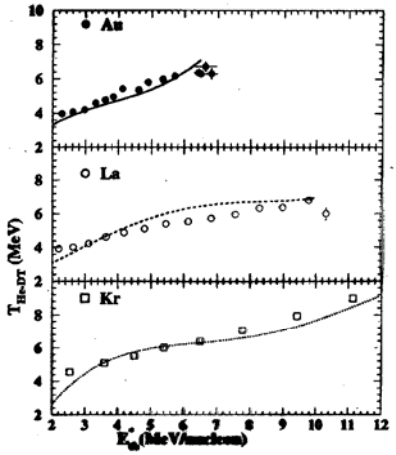

FIG. 19. Caloric curves (T_f vs E^*_{th}/A) for Kr, La, and Au. Points are experimental and curves are from SMM.

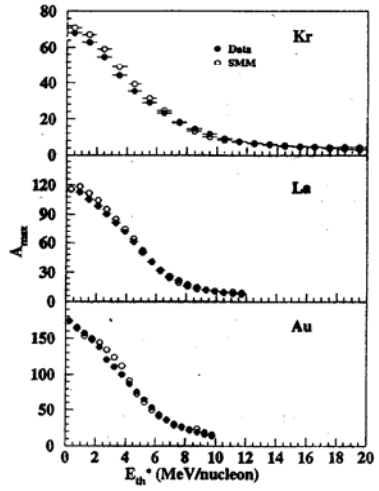

FIG. 7. Size of the largest fragment as a function of E^*_{th} for Kr, La, and Au from data and SMM.

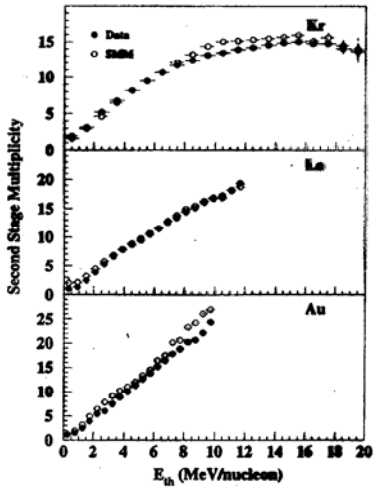

FIG. 6. Second stage charged-particle multiplicity as a function of E^*_{th} for Kr, La, and Au from data and SMM.

ALADIN

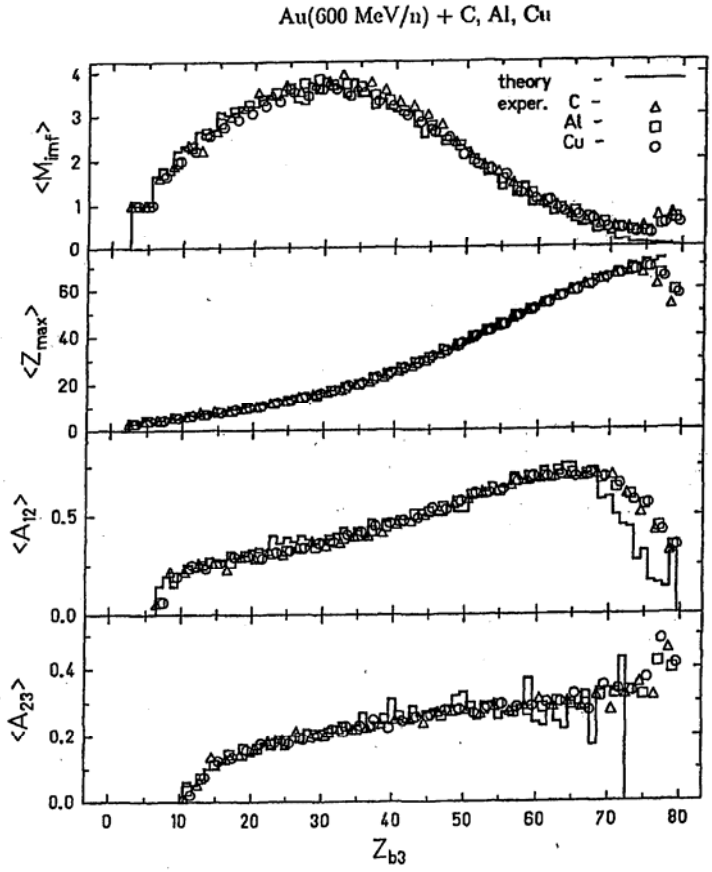

Fig. 7.13. Mean IMF multiplicity $\langle M_{imf}\rangle$, maximum fragment charge $\langle Z_{max}\rangle$, first $\langle A_{12}\rangle$ and second $\langle A_{23}\rangle$ fragment asymmetries (see text) versus the bound charge Z_{b3} in the reaction Au(600 MeV/nucleon) + Cu [189].

ALADIN data

Multifragmentation of spectators in relativistic HI c.

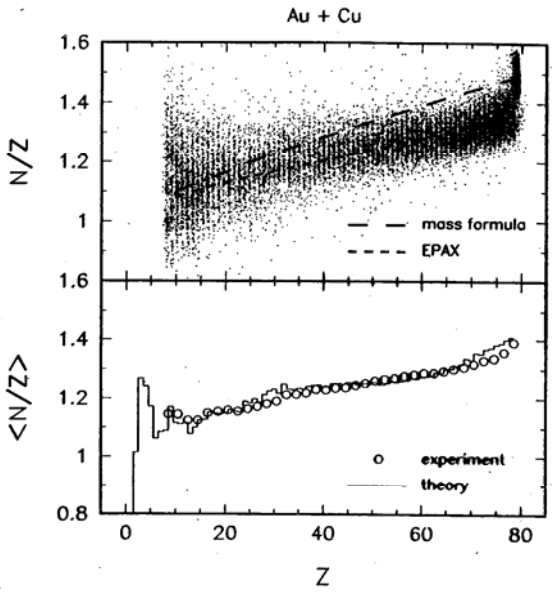

Fig. 3. Measured N/Z (top) and mean value $\langle N/Z \rangle$ (bottom) as a function of the atomic number Z of projectile fragments from the reaction ^{197}Au + Cu at E/A = 600 MeV. The lines in the top panel represent the valley of stability according to the Weizsäcker mass formula (long dashed) and the EPAX parameterization [16] (short dashed). In the bottom panel, the experimental data are given by the open circles and the prediction of the statistical multifragmentation model by the histogram.

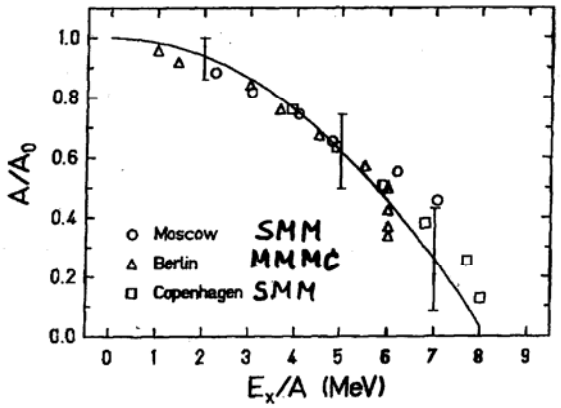

Fig. 4. Correlation of relative mass A/A_0 (A_0 = 197) and excitation energy E_x/A of thermalized nuclear systems produced after the nonequilibrium stage in the ^{197}Au+C, Al, Cu and Pb reactions at E/A = 600 MeV. The results of the analyses of the Moscow [12], Berlin [14] and Copenhagen [13] groups are given by circles, triangles and squares, respectively. The solid curve and the vertical bars represent the mean correlation (Eq. (2)) and the widths (Eq. (3)) of the ensemble as suggested in this work.

Z. Phys. A 359, 397–406 (1997)

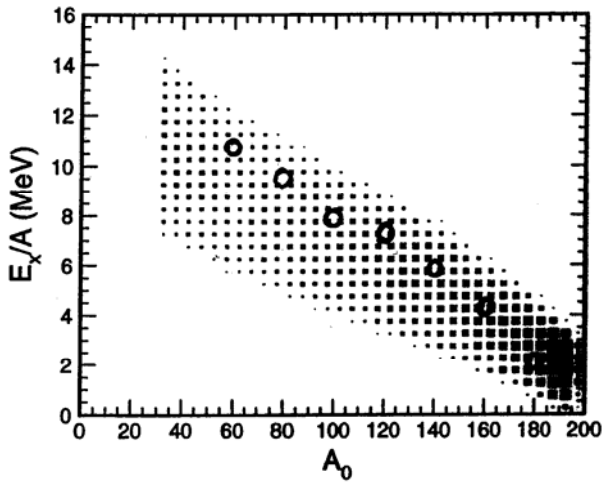

Fig. 8. Excitation energy E_x/A as a function of the mass A_0 for the ensemble of excited spectator nuclei used as input for the calculations with the statistical multifragmentation model. The *area of the squares* is proportional to the intensity

Description of ALADIN data

- SMM
- MMM (Raduta & Raduta, PR C61 (2000)

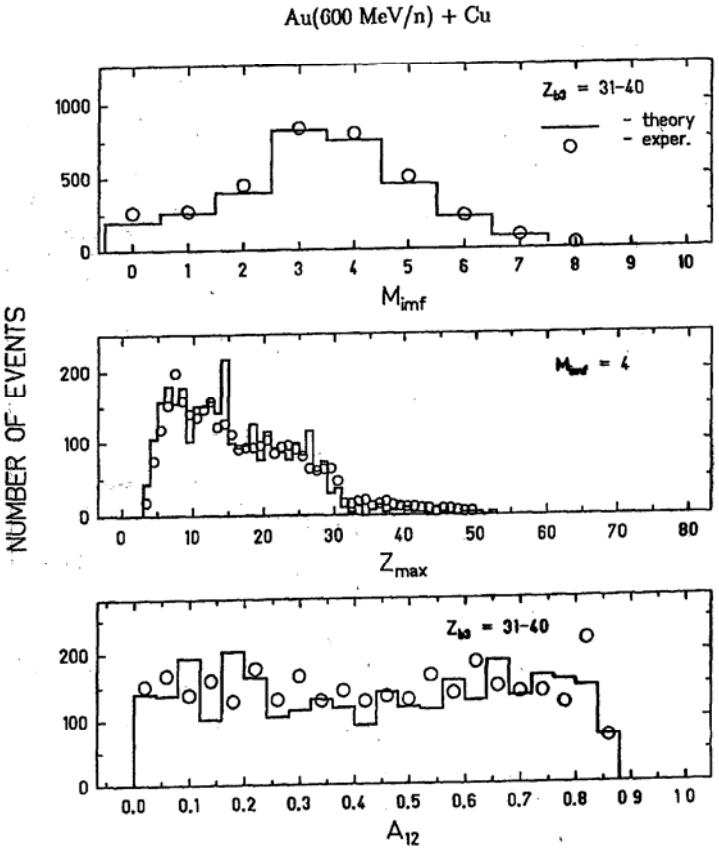

Fig. 7.14. Differential distributions of fragmentation events in the reaction Au(600 MeV/nucleon) + Cu [189]: in the IMF multiplicity for events with $Z_{b3} = 31$–40 (upper part); in the maximum fragment charge Z_{max} for events with $M_{imf} = 4$ (middle part); in the first fragment asymmetry A_{12} for events with $Z_{b3} = 31$–40 (lower part).

Principal component analysis

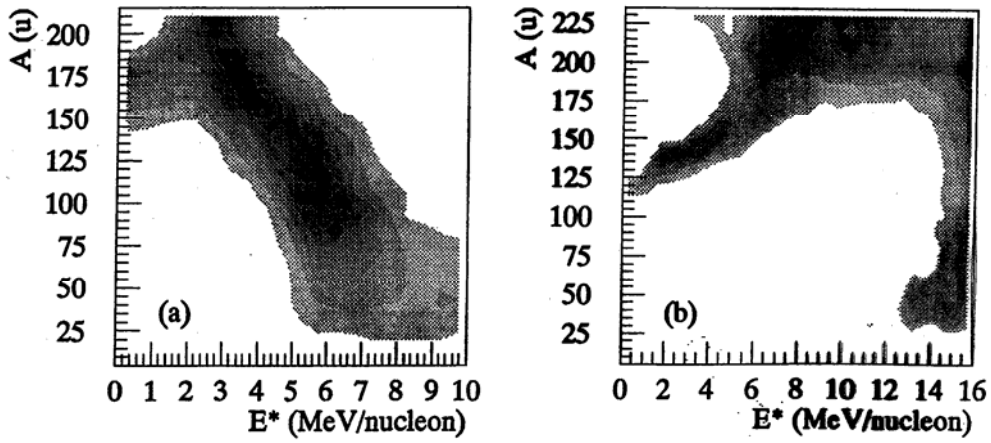

Fig. 4. Source variable correlated distributions $\mathcal{S}_{\infty}(E^*, A)$ for (a) the SMM model and (b) the Gemini model, corresponding to the ALADIN sample of events. The mass of the parent nucleus is denoted by A and its excitation energy by E^*. The observable CPDF used in the backtracing procedure is $\mathcal{O}_{\exp}(Z_{\mathrm{bg}}, M)$.

GSI: $^{12}C+^{112/124}$ Sn @ 300 A.MeV

Le Fevre et al.

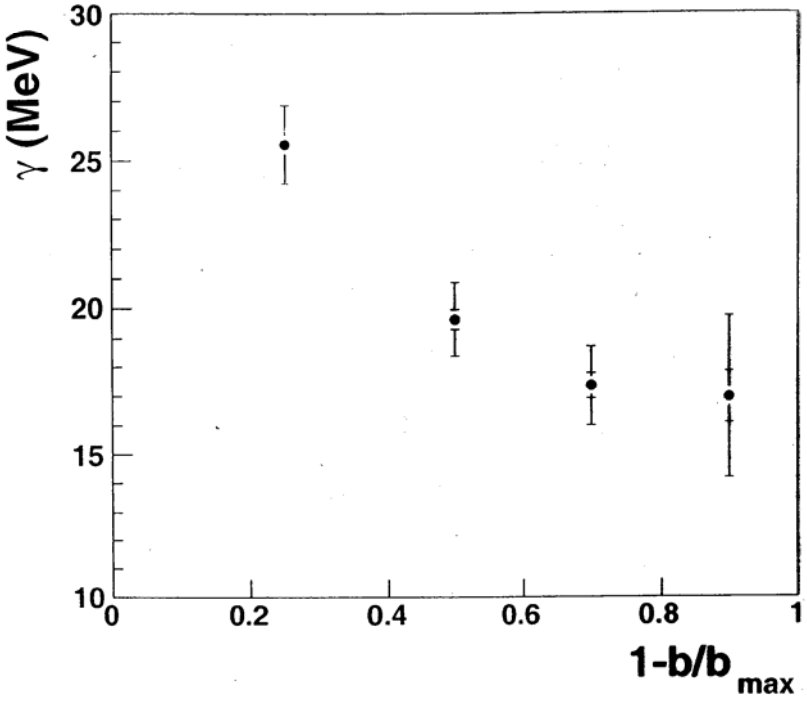

Symmetry energy: $E_{SYM} = \gamma \cdot (A-2Z)^2/A$

Isotopic scaling in (multi-)fragmentation:

$$Y_{AZ} \sim \exp\left[-\frac{1}{T}\left(F_{AZ}(T) - \mu A - \xi Z\right)\right]$$

for 2 sources with (A_1, Z_1) and (A_2, Z_2)

$$\frac{Y^1_{AZ}}{Y^2_{AZ}} \cong \exp\left[\frac{\mu_1-\mu_2}{T} A + \frac{\xi_1-\xi_2}{T} Z\right]$$

$$\boxed{\mu_1-\mu_2 \simeq -4\gamma\left[\left(\frac{Z_1}{A_1}\right)^2 - \left(\frac{Z_2}{A_2}\right)^2\right]}$$

D. Shetty et al.

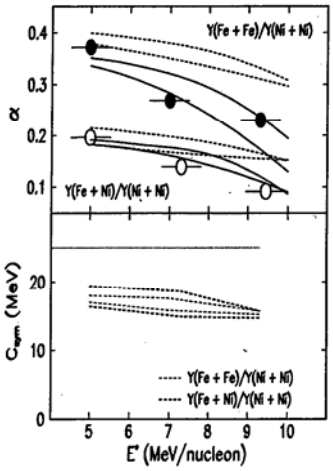

FIG. 5. Isoscaling parameter (top) and symmetry energy (bottom) as a function of excitation energy of the fragmenting source for the ^{58}Fe + ^{58}Ni and ^{58}Fe + ^{58}Fe reactions. (Top) The dashed and the solid curves are the calculated values of α from the primary and secondary fragment yield distributions using SMM, respectively. (Bottom) Symmetry energy calculated using the primary fragment yield distribution.

energy C_{sym} and given as follows (see Ref. [6]):

$$\alpha T = 4C_{sym}\left(\frac{Z_1^2}{A_1^2} - \frac{Z_2^2}{A_2^2}\right), \quad (5)$$

where Z_1, A_1 and Z_2, A_2 are the charge and the mass numbers of the fragmenting systems. Figure 5 (top panel) shows the experimentally determined (symbols) isoscaling parameter α from the reduced neutron density as a function of excitation energy of the fragmenting system. Also shown in the figure are the calculated values of the scaling parameter from the primary (dashed curve) and the secondary (solid curve) fragment yield distribution using the statistical multifragmentation model. Within the uncertainties in the input parameters of the SMM calculation, the decrease in the α values with increasing excitation energy is well explained by the calculation once the secondary deexcitation effect in the primary distribution is taken into account. Also, the calculated values from the secondary fragment distribution are not very different from those calculated from the primary fragment distributions for the lower excitation energies. However, with increasing excitation energy and isospin (N/Z) of the system they differ significantly. More specifically, the scaling parameter α for the neutron-rich primary fragments produced at excitation energies greater than 5–6 MeV/nucleon are strongly affected by the secondary decay effect.

Having demonstrated the fact that the observed scaling parameter is well reproduced by the statistical multifragmentation model and that a high degree of thermalization is expected during the fragment formation, we have attempted to obtain an estimate of the symmetry energy C_{sym} of the primary fragments using Eq. (5). The temperature for the estimate was determined using the double isotope ratio of the fragment yield [14]. Because the determination of the temperature from the fragment yield is also affected by the secondary deexcitation, a maximum correction of 70% was applied to be consistent with the previous determination of temperature for similar reactions (see Ref. [21]). This correction results in a temperature value of 6–7 MeV over the energy range studied. The difference $(Z/A)_1^2 - (Z/A)_2^2$ of the fragmenting system was estimated at $t = 50$ fm/c using the dynamical model calculations [10,17,22] and was about a 3% lower than the difference in the initial Z/A of the systems. Within these uncertainties, one obtains C_{sym} between 15 and 20 MeV over the excitation energy range studied. The estimated values from both the systems, ^{58}Fe + ^{58}Fe and ^{58}Fe + ^{58}Ni, are comparable to each other and shown by the thin and thick dashed lines in Fig. 5 (bottom). These observed values are significantly lower than the standard value of 25 MeV (dotted line) often assumed for a stable and unexcited nuclei. Furthermore, the symmetry energy is also observed to decrease slowly with increasing excitation energy. It should be mentioned that the estimated value of the symmetry energy is sensitive to the corrections assumed for the $(Z/A)_1^2 - (Z/A)_2^2$ in Eq. (5). A lower value of the $(Z/A)_1^2 - (Z/A)_2^2$ could raise the value of symmetry energy. An uncertainty in $(Z/A)_1^2 - (Z/A)_2^2$ of 30% could increase the symmetry energy value to about 19–20 MeV. However, it would require a correction of more than 70% at the highest excitation energy to reproduce the standard value of 25 MeV. Such an increase in not supported by any dynamical calculations and appears unlikely. It thus appears impossible to reproduce the standard value of the symmetry energy by any means. The data along with the calculations thereby suggests that the symmetry energy is below 20 MeV and well below the standard value. The reduced value of the symmetry energy shows that the primary fragments are not only excited and neutron rich but also expand to a reduced density when formed. For higher excitation energies the fragments appear to expand to even lower symmetry energies. A self-consistent check of the SMM calculation shows strong variations in the properties of the primary fragments when C_{sym} is varied in the range 15–25 MeV. Recently [5], it has been shown that neutron-rich hot nuclei can be produced in stellar matter between the protoneutron star and the shock front in a type II supernova explosion. In particular, it has been shown that a slight decrease in the symmetry energy coefficient can shift the mass distributions to higher masses. This property of hot nuclei could thus be interesting to investigate for understanding the relative abundance of elements in the core collapse supernovae explosion.

VI. CONCLUSION

In conclusion, we have studied the isotopic properties of the primary and secondary fragment yield distribution using the reduced nucleon densities in multifragmentation

Development of the statistical multifragmentation model (SMM).

Grand Canonics: density of fragments with mass A and charge Z in nuclear matter

$$\langle \rho_{AZ} \rangle = g_{AZ} \frac{V_f}{V} \frac{A^{3/2}}{\lambda_T^3} \exp\left[-\frac{1}{T} \left(F_{AZ} - \mu A - \xi Z \right) \right] \qquad (1)$$

Total density $\rho = M/V = \Sigma \langle \rho_{AZ} \rangle$, M is number of nucleons and V is volume of the system. The 'free' volume $V_f \approx V$.

g_{AZ} is the degeneracy of fragments, $\lambda_T = \left((2\pi\hbar^2)/(m_N T) \right)^{1/2}$ is the nucleon thermal wavelength.

μ and ξ are the chemical potentials for the nucleon number and charge conservation in the system.

Free energy of fragments:

$$F_{AZ} = F^B_{AZ} + F^S_{AZ} + E^C_{AZ} + E^{sym}_{AZ}$$

Bulk energy: $F^B_{AZ} = (-W_0 - T^2/\epsilon_0)A$,
$W_0 = 16$ MeV is the binding energy of nuclear matter, and
$\epsilon_0 = 16$ MeV is the inverse level density.

Surface energy: $F^S_{AZ} = B_0 A^{2/3} ((T_c^2 - T^2)/(T_c^2 + T^2))^{5/4}$,
$B_0 = 18$ MeV is the surface coefficient, and $T_c = 18$ MeV is the critical temperature of nuclear matter.

Coulomb energy: $E^C_{AZ} = cZ^2/A^{1/3}$,
in the Wigner-Seitz in the case of electro-neutrality
$c = (3/5)(e^2/r_0)(1 - 1.5(\rho/\rho_0)^{1/3} + 0.5(\rho/\rho_0))$, with r_0=1.17 fm.

Symmetry energy: $E^{sym}_{AZ} = \gamma(A - 2Z)^2/A$,
$\gamma = 25$ MeV is the symmetry energy parameter.

Reactions with leptons, in equilibrium:

$$e^- + p \rightarrow n + \nu_e$$
$$e^+ + n \rightarrow p + \bar{\nu}_e$$

(and inverse reactions, also with all nuclei)

Including electrons.

density of electrons: $\rho_e = \rho_{e^-} - \rho_{e^+}$

charge conservation (electro-neutrality): $\Sigma \rho_{AZ} Z = \rho_e$
share of electrons: $Y_e = \rho_e / \rho$

equilibrium: $\mu_e = -\xi$

Relativistic degenerate electron gas:

$$\rho_e = \frac{1}{3\pi^2} \left(\frac{\mu_e}{\hbar c}\right)^3 \left[1 + \mu_e^{-2} \left(\pi^2 T^2 - \frac{3}{2} m_e^2 c^4\right)\right]$$

Including electron neutrinos.

density of neutrinos: $\rho_\nu = \rho_{\nu_e} - \rho_{\bar{\nu}_e}$

conservation of leptons: $Y_{lept} = (\rho_e + \rho_\nu)/\rho = const$

equilibrium: $\mu_e - \mu_\nu = -\xi$

$$\rho_\nu = \frac{1}{6\pi^2} \left(\frac{\mu_\nu}{\hbar c}\right)^3 \left[1 + \mu_\nu^{-2} \pi^2 T^2\right]$$

Self-consistent calculation of all densities ρ_{AZ}, ρ_e, and ρ_ν !

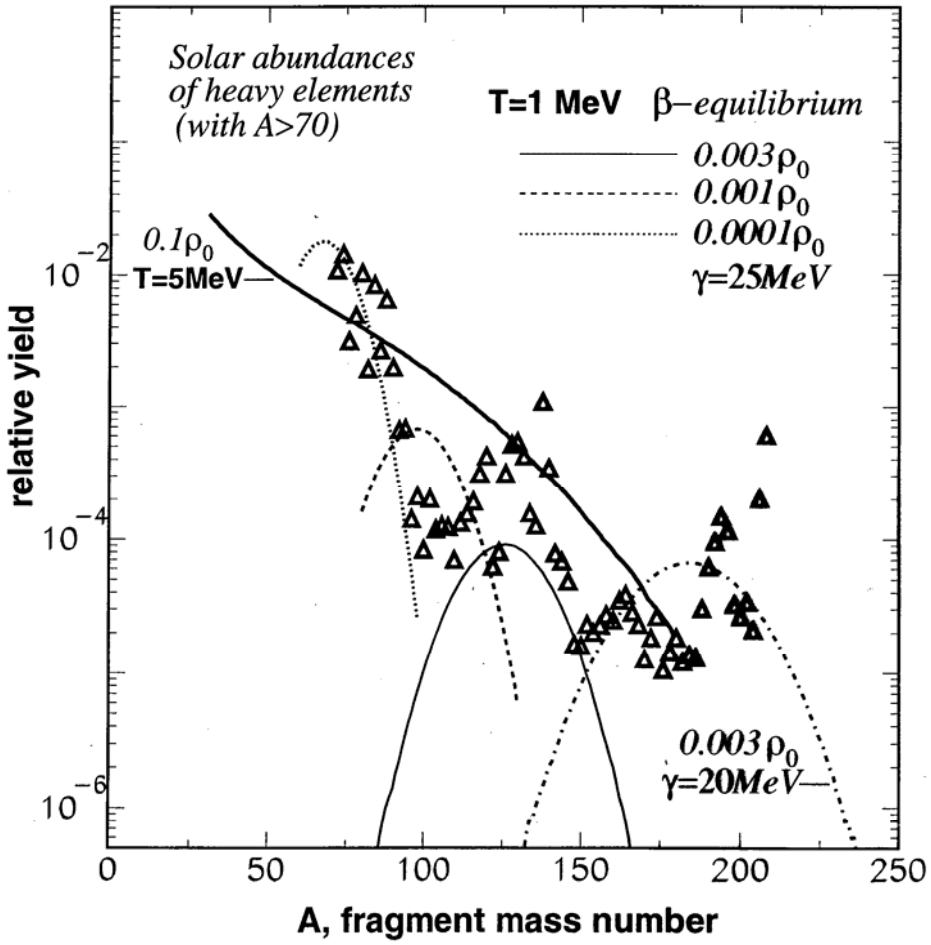
Solar abundances
of heavy elements
(with A>70)
T=1 MeV β–equilibrium
0.003ρ0
0.001ρ0
0.0001ρ0
γ=25MeV
0.1ρ0
T=5MeV
0.003 ρ0
γ=20MeV
relative yield
10−2
10−4
10−6
0
50
100
150
200
250
A, fragment mass number

Application of statistical models of nuclear multifragmentation:

- Hybrid calculations of particle transport in complex matter: nuclear transmutation (environment), electro-nuclear breeding (new methods of energy production), proton and ion therapy (medical research), radiation defense of space detectors (space research). The process of multifragmentation take as much as 10-15% of the **total** cross section in high-energy hadron-nucleus reactions, and much more for **high**-energy nucleus-nucleus collisions. Multifragmentation can be a dominating **channel** for production of some particular isotopes.

- As part of investigation of the phase diagram of nuclear matter: determination of properties of hot nuclei/fragments (e.g. their symmetry energy) produced in multifragmentation reactions. Influence of surrounding matter on the fragment properties. Important astrophysical consequences.

- Mathematical methods of statistical multifragmentation can be used for development of thermodynamics of finite systems. Links with cluster physics, condensed matter physics, ...